Thermal-strain Enabled Enhanced Emission from UV

Laser-induced Defect Levels near the Surface of

Multilayer MoS<sub>2</sub>

Sinto Varghese <sup>1</sup>, Noah Hurley <sup>1</sup>, Steve Kamau <sup>1</sup>, Yan Jiang <sup>1</sup>, Roberto Gonzalez Rodriguez <sup>1</sup>,

Bhojraj Bhandari <sup>1</sup>, Tengteng Lyu <sup>2</sup>, Hao Yan <sup>2</sup>, Yuanxi Wang <sup>1</sup>, Anupama B. Kaul <sup>3,4</sup>, Jingbiao

Cui, and Yuankun Lin 1,3\*

<sup>1</sup>Department of Physics, University of North Texas, Denton, TX 76203, USA

<sup>2</sup>Department of Chemistry, University of North Texas, Denton, TX 76203, USA

<sup>3</sup>Department of Electrical Engineering, University of North Texas, Denton, TX 76203, USA

<sup>4</sup>Department of Materials Science and Engineering, University of North Texas, Denton, TX, USA

\* Corresponding author

E-mail: yuankun.lin@unt.edu

Abstract

Monolayer two-dimensional (2D) materials have been intensively studied while research on

multilayers is still in its infancy. Here, we induce defects inside bulk MoS2 through thermal

annealing and near the surface of multilayer MoS<sub>2</sub> using 375 nm laser irradiation, and investigate

1

their photoluminescence (PL) and fluorescence lifetime imaging (FLIM). Enhanced emission is limited within a certain MoS<sub>2</sub> thickness. The observed enhanced emission is evidenced by a threshold behavior in super-linear PL intensity increase, strong polarization effects, and increased lifetime of defect peak. The laser power threshold for enhanced emission is much smaller in defects near the surface than that inside the bulk of multilayer MoS<sub>2</sub>. The mechanical strain from a wrinkle of the sample further lowers the laser power threshold for enhanced emission. By exciting with a 639 nm laser that is close to the fundamental gap between the conduction band minimum and the valence band maximum, the lifetime of defect enhanced emission increased by 5 times. Furthermore, one of the competing indirect bandgap emissions disappears, and the defect emission peak dominates the PL spectrum in the wrinkle area with a strain. The discovered principle can be applied to future studies on the integration of enhanced emission and single photon emission involving selectively depopulating the conduction band of the host crystal to defect levels for quantum emitters.

**Keywords:** Photoluminescence, Raman, MoS<sub>2</sub>, defect level, enhanced emission, fluorescence lifetime imaging, 2D materials

#### Introduction

The advent of two-dimensional (2D) materials has revolutionized the field of nanomaterials, offering unique properties such as high integration density, tunable electronic and optical characteristics, and robust light-matter interactions<sup>1–3</sup>. These materials exhibit intriguing possibilities due to their point defects, which can bestow them with a diverse array of functionalities, including tunable electrical conductivity<sup>4</sup>, ferromagnetism<sup>5</sup>, memristive behavior<sup>6–8</sup>, and the ability to serve as strain-controlled single photon emitters (SPE) <sup>9–11</sup>. In the quest to

harness the full potential of these defects, researchers have primarily focused on 2D monolayers, where defect emission properties have been thoroughly explored <sup>12–14</sup>. SPEs have been discovered in defect states of monolayer transition metal dichalcogenides (TMDs) and h-BN monolayers mechanically exfoliated or grown by chemical vapor deposition, such as MoS<sub>2</sub> <sup>15,16</sup>, MoSe<sub>2</sub><sup>12,17</sup>, WSe<sub>2</sub> <sup>1,3,18,19</sup>, WS<sub>2</sub> <sup>20,21</sup>, MoTe<sub>2</sub> <sup>22</sup>, and h-BN <sup>11,23,24</sup>. SPEs have also been observed from multilayer samples of GaSe <sup>25,26</sup>, h-BN<sup>24</sup>, and oxidized WS<sub>2</sub> (i.e.WO<sub>3</sub>)<sup>27</sup>. SPE behavior and a zero-phonon line clearly separated from phonon sidebands were observed in multilayer h-BN<sup>24</sup>.

The practical utility of these defects in monolayers is often hindered by their susceptibility to oxidation under ambient conditions<sup>28</sup>, limiting their long-term stability and potential as single photon emitters. The pursuit of technologically desirable defects has led to the exploration of multilayer TMDs, which offer a unique advantage: the ability to embed defects beneath the sample surface, ensuring their long-term stability as single photon emitters. In a thermal-annealed multilayer MoS<sub>2</sub>, the defects embedded inside the bulk can survive under high laser power and the defect induced PL peak (D-peak) shows a superlinear intensity increase starting at 17 mW<sup>29</sup>.

Although our previously observed defect emission behavior in bulk MoS<sub>2</sub> under thermal strain is striking <sup>29</sup> – including strong polarization effects and anomalously strong intensities – the puzzle remains as to why has this defect not been reported so far, especially considering that TMD optical properties have garnered the spotlight of 2D research for more than a decade. There are the following two considerations. (1) The focus of past work on few-layer and monolayer TMD requires laser powers below ~1 mW to avoid thermal effects and irreversibly damaging the TMDs sheets <sup>30</sup>. Stronger laser powers in the range of 5– 20 mW lead to surface adsorption or even thinning and etching <sup>30–33</sup>. By contrast, bulk MoS<sub>2</sub> is more resilient to laser irradiation, where laser-

induced heat may distribute throughout the bulk and dissipate more efficiently<sup>30</sup>. This enables us to probe bulk MoS<sub>2</sub> defect emission non-destructively under strong laser powers, contrary to laser power restrictions usually prescribed for monolayers. (2) Out of the two sets of sulfur vacancy levels – one unoccupied set in the bandgap and another occupied level near the valence band edge - the latter is typically lower in energy than the valence band local maximum at the K point in monolayer and bulk MoS<sub>2</sub> <sup>34</sup>. In monolayer MoS<sub>2</sub>, this occupied level is not known to move above the valence band maximum (VBM) at K under moderate strain (<5%) 35. By contrast, we previously showed that this occupied level moves above the VBM at K under only 2% thermal strain (see e.g. Fig. S11 of Reference<sup>29</sup>). This in turn sets up an effective two-level system that allows direct interband emission between the unoccupied and occupied sulfur vacancy levels, without participation of the bulk valence band edge at K (the other valence band valley at  $\Gamma$  has a much smaller optical matrix element with the midgap state). It is the unconventional combination of strong laser power applied non-destructively to bulk MoS<sub>2</sub> and the occupied vacancy level lifting off from the VBM under strain (unique to bulk MoS<sub>2</sub>) that enables strong emission intensities and polarization effects in activated sulfur vacancies at room temperature.

In this study, to further verify previous theory predictions and exact conditions for the enhanced emission, we design and produce S vacancies deep inside multilayer MoS<sub>2</sub> using two methods: thermal annealing introduces defects uniformly in bulk MoS<sub>2</sub>, and UV 375 nm laser irradiation induces defects near the surface of bulk MoS<sub>2</sub>. By applying both thermal and mechanical strain, enhanced emission occurs at much lower laser power for defects near the surface than those inside the bulk. The defect (D) peak dominates in the PL spectrum while the indirect bandgap emission disappears. The lifetime of D peak increases by 5 times when it is excited from VBM to conduction band minimum.

### **Experimental methods**

Preparation of defects through thermal annealing: A free-standing thick MoS<sub>2</sub> was exfoliated by contacting a scotch tape at the edge of bulk MoS<sub>2</sub> (2D Semiconductor) and peeling off. The peeled sample was pressed onto copper-coated glass by polydimethylsiloxane (PDMS). It was annealed at 180 °C for 3 hrs on a hot plate and then rapidly cooled to 0 °C in a fridge for 3 minutes<sup>29</sup>. Then the sample was put in an ultrasonic vibration where the uppermost loose layers were removed. Thickness measurements were performed through profilometer analysis.

### Preparation of defects through 375 nm laser irradiation:

Multilayer MoS<sub>2</sub> with a thickness of 86 nm was obtained by the exfoliation of bulk MoS<sub>2</sub> (2D Semiconductor). The exfoliation process involved the use of scotch tape and thermal release tape as the final step. We then placed the exfoliated multilayer MoS<sub>2</sub> onto a copper-glass substrate and pressed it with PDMS. The substrate, with the attached material, underwent heating at 100°C until the thermal release tape released the sample onto the substrate. The MoS<sub>2</sub> was then irradiated with UV 375 nm laser (2 mm beam size, 8 mW) for 6 minutes. Thickness and wrinkle profiles were performed in the beam profilometer. Because MoS<sub>2</sub> is not transparent to 375 nm, the UV 375 nm laser irradiation generates defects near the surface of multilayer MoS<sub>2</sub>.

Raman and Photoluminescence Spectra: Most of Raman and photoluminescence (PL) spectra measurements were carried out at room temperature using a Renishaw inVia Raman Microscope. We employed an 1800 lines/mm grating for these measurements, covering a wavelength range of up to 950 nm. For the PL measurement covering wavelengths up to 1050 nm, we employed a 1200 lines/mm grating. Throughout these measurements, a Cobolt Samba 532 nm laser was utilized,

coupled with a 50× objective lens (numerical aperture NA=0.5) with a working distance of 8.2 mm. Precise laser power adjustments on the sample were achieved through a combination of neutral density filters and laser power control software provided by Cobolt Samba. The exposure time remained consistently set at 10 seconds. Notably, 1 mW of laser power corresponded to a laser intensity of 0.59 kWcm<sup>-2</sup>, based on our optical setup; hereafter we use laser power instead of laser intensity to document our results. To explore Raman and PL polarization effects, a broadband polarizing beam splitter cube (Thorlabs) was introduced into the optical path of the Renishaw inVia, effectively handling scattered light. This adjustment was necessitated by the fact that the built-in polarizer in the Raman spectrometer had been optimized for Raman polarization near the 532 nm wavelength. We also studied the Raman and PL measurement at room temperature using 633 nm laser coupled with a 50× objective lens (numerical aperture NA=0.5). A heating/cooling stage (Linkam THMS600) was mounted on the microscope for in-situ low-temperature Raman and PL analysis.

Fluorescence Lifetime Imaging (FLIM): The fluorescence lifetime imaging (FLIM) and its lifetime histogram for A-peak and D-peak in the sample of defects near the surface of multilayer MoS<sub>2</sub> were measured in a Micro Time 200 time-resolved confocal fluorescence microscope. Photon detection events were meticulously recorded using a PicoQuant PicoHarp 300 time-correlated single-photon-counting system. Two Picosecond(PS) lasers were used for the excitation of PL. One picosecond laser has a wavelength of 639 nm, a repetition rate of 80 MHz, and an average power of 1.63 mW. The other has a wavelength of 405 nm, a repetition rate of 80 MHz, and an average power of 3.84 mW. The confocal microscope was equipped with a 20× objective lens (numerical aperture NA=0.4). The confocal microscope used a 20× objective lens (numerical aperture NA=0.4) with a working distance of 12.0 mm. To reduce the height variation effect

around the wrinkle, the piezo-stage was set to scan the crest of the wrinkle. Scanning a large area results in the variation of lifetime event number. Data acquisition and subsequent analysis were seamlessly executed using SymPho-Time 64 software.

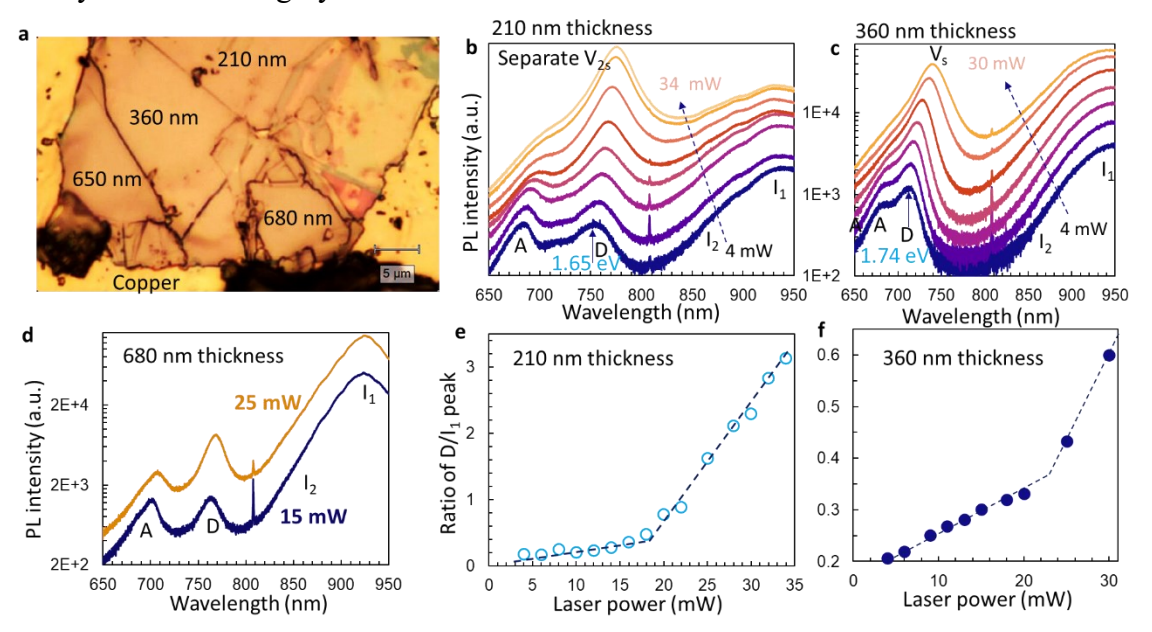


**Figure 1.** (a) Optical image of Multilayer MoS<sub>2</sub> sample with various thickness regions with embedded thermal defects. (b) PL spectra under laser powers of 4, 8, 12, 16, 20, 25, 32, and 34 mW for sample thickness of 210 nm. (c)PL spectra under laser powers of 4, 6, 9, 13, 18, 25, and 30 mW for sample thickness of 360 nm. (d) PL spectra under laser powers of 14 and 25 mW for sample thickness of 680 nm. (e-f) Ratio of D peak to I peak, computed via peak fitting, as a function of laser powers for regions with thicknesses of 210 nm (e) and 360 nm (f).

#### Results of PL measurement and enhanced emission in thermally annealed MoS<sub>2</sub>

In this section, we focus on the first type of defective samples obtained by thermal annealing and explore the relationship between the thickness of our multilayer MoS<sub>2</sub> sample and the enhanced emission arising from defects. Figure 1a shows an optical image of the multilayer MoS<sub>2</sub> sample, showcasing various thickness regions obtained through profilometer analysis. Laser power dependent PL spectra across three different regions of the sample, as depicted in Figures 1b, 1c, and 1d, corresponding to thicknesses of 210 nm, 360 nm, and 680 nm, respectively. In Fig.

1b and 1d, the D peak is around 751 nm (1.65 eV) excited by a low laser power, associated with a defect that has been tentatively attributed to V<sub>2S</sub> (di-sulfur vacancy) following the calculated bandgaps of the oxygen passivated S-defects in Table S2 in the supporting information of a reference <sup>28</sup>. The D peak in Fig. 1c is around 713 nm (1.74 eV), which we attribute to Vs (sulfur vacancy) following the atomic force microscopy (AFM) images<sup>34</sup>, comparison of PL measurement and density functional theory (DFT) calculations <sup>29,34</sup> (also in Table S2 of the reference<sup>28</sup>). All samples and defects survive under high laser powers up to 34 mW. The PL intensities of the A-peak (free exciton peak) and I<sub>1</sub> peak (indirect bandgap emission) increase linearly with the laser power<sup>29</sup>. There is no enhanced emission from the sample with a thickness of 680 nm in Fig. 1d as the ratio of the D peak intensity over the I<sub>1</sub>-peak intensity is the same under 15 and 25 mW.

Figs. 1e and 1f illustrate the intensity ratio of D-peak over I<sub>1</sub>-peak, computed via peak fitting, for regions with thicknesses of 210 nm and 360 nm. The intensity ratio shows two linear increase regions fitted with two different slopes, as indicated by the dashed line in Fig. 1e for 210 nm thickness. The D-peak is considered to exhibit enhanced emission, initiating at a laser power threshold of 19 mW. This transition was previously attributed to the Kc valley replacing the Qc valley as the CBM as it becomes populated by carriers, relaxing them from Kc valley to defect levels, and consequently leading to enhanced emission in three-level energy system<sup>29</sup>. A similar intensity ratio with two distinguished regions occurs in Fig. 1f for the sample with a thickness of 360 nm. The enhanced emission of D peak is triggered at a laser power of 24 mW. These results underscore the profound influence of sample thickness on the thermal strain-enabled enhanced emission. Specifically, thinner multilayer samples (210 nm) exhibit enhanced emission at relatively lower laser powers (19 mW), while the 360 nm sample, although exhibiting enhanced

emission, did so at higher laser powers (24 mW). Notably, the 680 nm thick region failed to manifest enhanced emission even under the influence of higher laser power (25 mW).

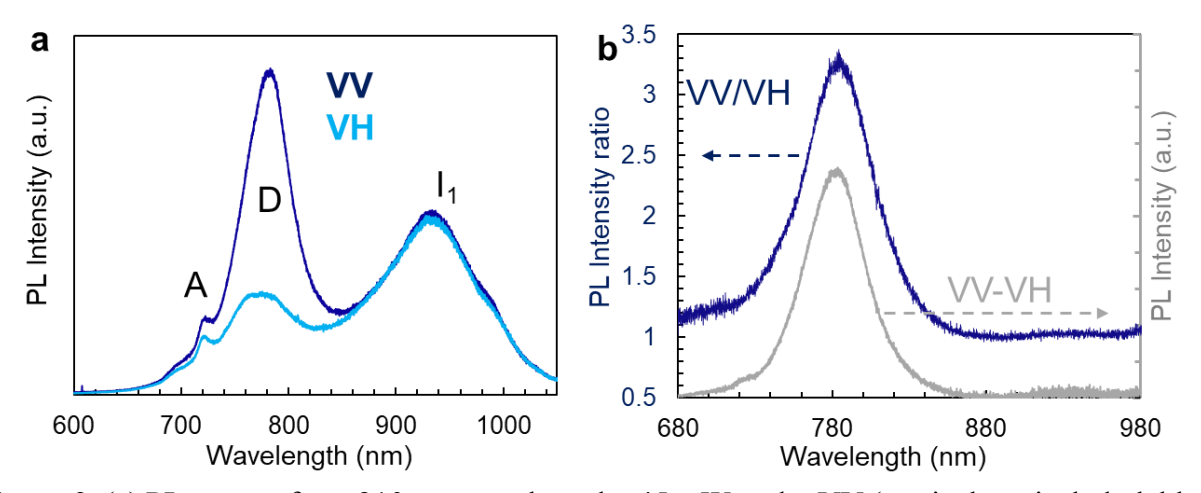


**Figure 2.** (a) PL spectra from 210 nm sample under 45 mW under VV (vertical vertical, dark blue) and VH (vertical horizontal, light blue) setups, where their intensities normalized relative to I<sub>1</sub>. (b) The spectral ratio VV/VH and difference VV-VH for 210 nm sample.

We checked the Raman spectrum under laser power of 4 mW and 25 mW as shown in Fig. S1a for the sample thickness of 210 nm and in Fig. S1b for 360 nm. The Raman E<sub>2g</sub> and A<sub>1g</sub> peak wavenumbers change by 3.02 and 2.67 cm<sup>-1</sup> for the sample with a thickness of 210 nm, respectively, when the laser power is changed from 4 mW to 25 mW. For the sample with a thickness of 360 nm, E<sub>2g</sub> and A<sub>1g</sub> peak wavenumbers change by 3.22 and 2.87 cm<sup>-1</sup> for laser power from 4 mW to 25 mW. Usually the Raman peak red-shifts with increasing temperature from lattice thermal expansion<sup>29</sup>. It means the thicker sample (360 nm) may have a higher temperature than the 210 nm sample, due to more absorption in a thicker sample. The defect type is the same in Fig. 1b and 1d so we compare the Raman peak under the laser power of 25 mW. The Raman E<sub>2g</sub> and A<sub>1g</sub> peaks are located at 380.69 and 406.55 cm<sup>-1</sup>, respectively, for 210 nm thickness, while they are at 380.35 and 405.97 cm<sup>-1</sup> for 680 nm thickness. Again, this may be attributed to the thicker sample (680 nm) having a higher temperature. Considering both temperature and thickness effect, the sample thickness plays a crucial role in the observation of enhanced emission.

We also measured the polarization effect for the 210 nm sample under a laser power of 45 mW. Fig. 2a shows normalized PL spectra relative to the I<sub>1</sub> peak for polarizations of VV (vertical excitation, vertical scattered signal) and VH (vertical excitation, horizontal scattered signal). The A, D, and I<sub>1</sub> peaks are clearly separated in Fig. 2a. The ratio of the VV spectrum over VH and the difference of VV and VH spectra are shown in Fig. 2b. Polarization effects can be seen wherever the ratio deviates significantly from unity. Clearly, VV/VH and VV-VH curves have peaks centered at D-peak. There is no feature at wavelengths for A and I<sub>1</sub> peaks. As seen from Fig. 2, the D-peak in the PL spectra is highly polarized, presumably due to it originating from enhanced emission.

#### Results from MoS2 with defects induced by UV laser irradiation

Next, we focus on the second type of defective samples obtained by UV laser irradiation. The thickness of the multilayer MoS<sub>2</sub> sample is determined to be 86 nm using profilometer as

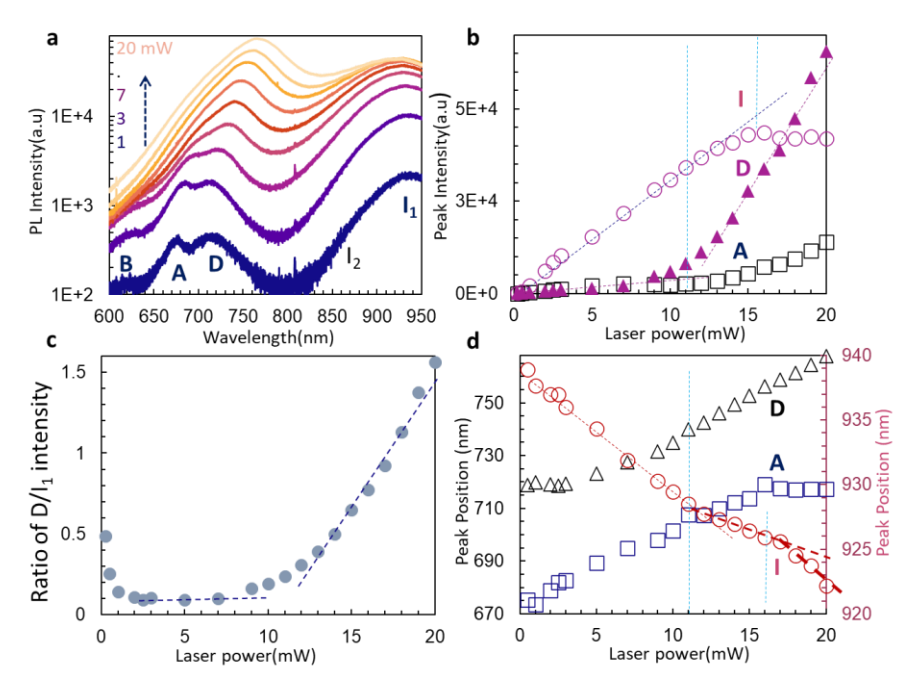


**Figure 3.** (a) PL spectra of UV laser irradiation-induced defects in flat multilayer MoS<sub>2</sub> under laser powers of 1, 3, 7, 10, 12, 14, 16, 18, and 20 mW from bottom to top. (b) PL peak intensity for A-peak (squares), D-peak (tringles), and I-peak (circles) as a function of laser power. (c) The ratio of D peak to I<sub>1</sub> peak intensity, computed via peak fitting, as a function of laser powers. (d) PL peak positions as a function of laser power where primary axis represents the peak positions for D-peak and A-peak, and secondary axis represents the peak position for I<sub>1</sub>-peak.

shown in Fig. S2a for the optical image and in Fig. S2b for the height profile. A wrinkle in the sample can be seen in the bottom right corner of Fig. S2a and is characterized separately in Fig. S3. Figures S3a and S3b show the optical image and height profile for this wrinkle in the sample, respectively. The wrinkle has a height of 3.53 µm and a width of 27.1 µm as shown in Fig. S3b where PL and FLIM were taken. After the sample is irradiated by UV 375 nm laser for 6 minutes,

S vacancies have been generated. For the long-term stability of defects and for data management purposes, we coated the sample with 30 nm Al<sub>2</sub>O<sub>3</sub> by atomic layer deposition at 150 °C.

The D peak at the flat sample region has a wavelength of 718.8 nm at 0.5 mW. Fig. 3a shows the PL spectra at a flat multilayer MoS<sub>2</sub> region under different laser powers of 1, 3, 7, 10, 12, 14, 16, 18, and 20 mW. The A and B peaks (both from free excitons), D peak, and I peak are observed. Notably, for lower laser powers, the I-peak exhibited higher intensities compared to the D-peak. As the laser power increased, the D-peak intensity surpassed that of the I peak. We presented peak-fitted data in Figures 3b and 3c, illustrating laser power-dependent PL intensities and their ratio, and in Figure 3d, illustrating power-dependent PL peak positions. From Figure 3b, both the A-peak (squares) and the I-peak (circles) exhibited linear growth from 1 to 15 mW, whereas the D-peak (triangles) demonstrated a super-linear increase. Enhanced emission occurs above a laser power of approximately 11 mW, again attributed to efficient relaxation of carriers from K<sub>C</sub> valley to defect levels which cause population inversion in the defect level<sup>29</sup>. Due to the cross-over of Kc and Qc valley (Qc valley is higher in energy than the Kc valley after the transition), the steady-state carrier population becomes depleted in Qc valley, which decreases I<sub>1</sub> intensity. That is exactly what we have observed for I intensity above 15 mW (indicated by the second dashed blue line in the vertical direction). The ratio of D/I<sub>1</sub> intensities in Fig. 3c also shows the laser power threshold of 11 mW for the enhanced PL emission.

We next fitted the PL spectrum to extract wavelengths of all peaks. As seen from Fig. 3d, the wavelengths of the A peak (squares) and the D peak (triangles) increase with the increasing laser power due to laser-induced thermal strain, as predicted previously by density functional theory calculations<sup>29</sup>. At the threshold laser power of 11 mW, the D peak wavelength is 740 nm,

almost the same as the calculated threshold wavelength of 738 nm. The decreasing of I-peak wavelength slows down after 11 mW in Fig. 3d after the cross-over of K<sub>C</sub> and Qc valley, as indicated by dashed red lines for slopes.

We also studied the shift in Raman peaks of  $E_{2g}$  and  $A_{1g}$  as we increased the laser power in Figure S4. Increasing the laser power from 0.5 to 11 mW (starting point for the enhanced emission),  $E_{2g}$  and  $A_{1g}$  peak wavenumbers changed by 3.52 and 3.27 cm<sup>-1</sup>, indicating an effective temperature increase locally under laser irradiation by 265  $K^{2g}$ . The increased thermal strain enables the cross-over of  $K_C$  and  $Q_C$  valley, leading to enhanced emission<sup>29</sup>.

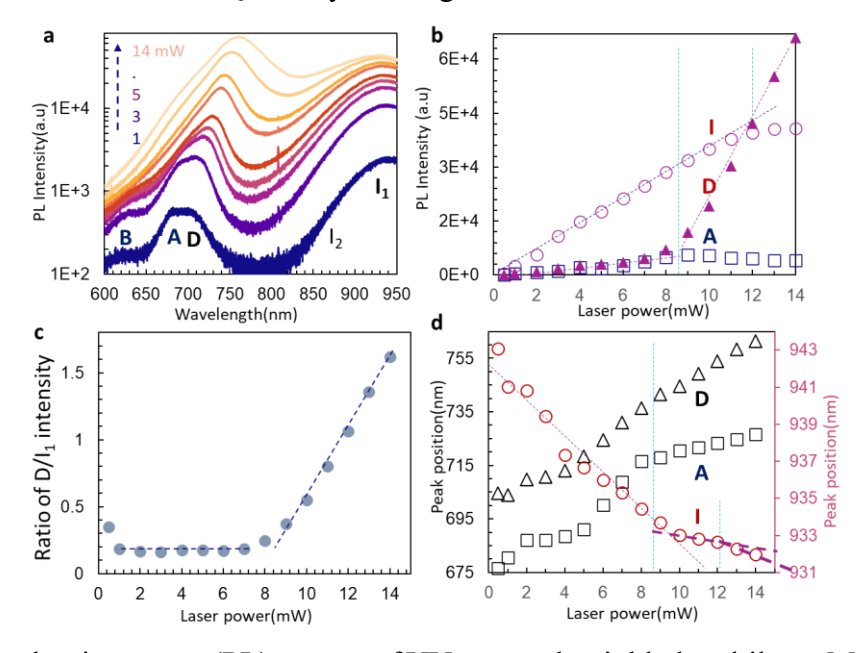


**Figure 4.** (a) Photoluminescence (PL) spectra of UV exposed wrinkled multilayer MoS<sub>2</sub> at various laser powers of 1, 3, 5, 6, 7, 9, 10, 12, and 14 mW from bottom to top using 523 nm Laser. (b) PL peak intensity for A-peak (squares), D-peak (triangles), and I peak (circles) as a function of laser power. (c) The ratio of D peak to I<sub>1</sub> peak intensity, computed via peak fitting, as a function of laser powers. (d) Peak positions as function of laser power where primary axis represents the peak positions for D-peak and A-peak, and secondary axis represents the peak position for I-peak.

To understand the effect of mechanical strain, we then studied PL on a wrinkle in our multilayer MoS<sub>2</sub> sample. It is a naturally formed wrinkle that occurred during the squeezing of air

between MoS<sub>2</sub> and substrate. The D peak on the wrinkle has a wavelength of 704.7 nm (1.76 eV) at 0.5 mW, same wavelength as the one produced by UV lamp <sup>28</sup>. Figure 4a shows the PL spectra on the wrinkle at various laser powers of 1, 3, 5, 6, 7, 9, 10, 12, and 14 mW. Similar to the flat region discussed above, the two free exciton peaks A and B, defect peak D, and indirect bandgap peak I are observed. Also similar is the D peak surpassing the I peak in intensity at high laser powers as observed in the flat region. To get a clearer picture of this phenomenon, we present the peak fitted data in Figures 4b and 4c indicating the laser power-dependent PL peak intensity and their ratio, and in Figure 4d, the laser power-dependent PL peak position. From Figure 4b, we noticed a linear increase in PL peak intensity for the A peak (square) and I peak (circle) from 1 to 10 mW whereas the D peak (triangles) showed super-linear behavior with increasing laser power. From the D peak intensity change, the enhanced emission can be estimated to start at 8.5 mW. The laser power threshold of 8.5 mW for the enhanced PL emission is also confirmed in the ratio of  $D/I_1$  intensities in Fig. 4c. Due to the mechanical strain from the wrinkle in addition to the generated thermal strain, the laser power required to enable enhanced emission in the wrinkle is lower than that in the flat region. It corresponds to lower laser power of 8.5 mW for the enhanced emission in Fig. 4b than 11 mW in Fig. 3b. In multilayer MoSe<sub>2</sub>, the threshold laser power is near 2 mW when the MoSe<sub>2</sub> is under both thermal and mechanical strain<sup>36</sup>. Above 12 mW laser power in Fig. 4b, the I peak intensity increases sub-linearly, indicated by the second vertical blue line. It is again due to strain enabled shifting of the Q<sub>C</sub> valley above K<sub>C</sub> valley.

The fitting of the PL spectrum gives D peak wavelength of 738.9 nm on average and A peak wavelength of 718.0 nm at 8.5 mW laser power in Fig. 4d, almost the same as the previously calculated values of 738 and 717 nm, respectively, at 1% strain. The decreasing of I peak wavelength slows down after the threshold laser power of 8.6 mW after the cross-over of K<sub>C</sub> and

Qc valley, as indicated by dashed red lines for slopes in Fig. 4d. We also studied the shift in Raman peaks of  $E_{2g}$  and  $A_{1g}$  as we increased the laser power in Figure S5. Increasing the laser power from 0.5 to 9 mW,  $E_{2g}$  and  $A_{1g}$  peak wavenumbers change by 4.52 and 3.98 cm<sup>-1</sup>, indicating an increase in the effective local temperature by 331  $K^{29}$ .

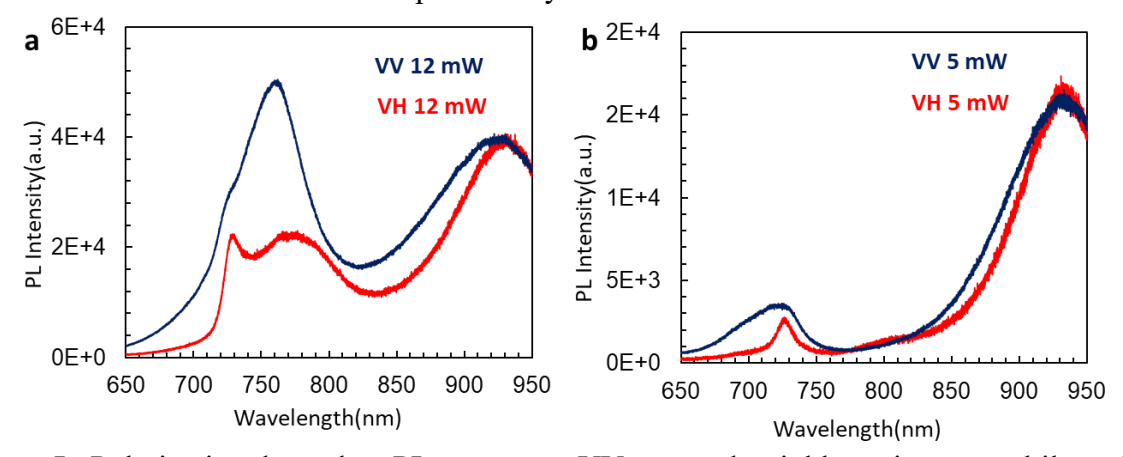


**Figure 5.** Polarization dependent PL spectra on UV exposed wrinkle region on multilayer MoS<sub>2</sub> with 532 nm laser, at 12 mW (a) and 5mW (b) under VV (blue) and VH (red) setups, where their intensities normalized relative to the I-peak.

To confirm that the enhanced emission started at the laser power of 8.5 mW on the wrinkle, studies<sup>29,37</sup>. conducted polarization We examined we the polarization-dependent photoluminescence (PL) spectra at two laser powers one below the threshold (5 mW), and one above the threshold (12 mW). Figures 5a and b illustrate the polarization-dependent PL spectra acquired at 12 mW and 5 mW, respectively on the wrinkle. We aligned the I peak of the spectra from both vertical-vertical (VV, blue) and vertical-horizontal (VH, red) polarization setups. From Figure 5a, it is evident that the intensity of the D peak (760 nm) for VH (red) is notably lower than the intensity of the D peak (760 nm) for VV (blue) at 12 mW. Conversely, Figure 4b shows that the VV (blue) and VH (red) curves exhibit similar D peak (730 nm) intensities at 5 mW. We did peak fitting for both graphs and checked the intensity ratio of the D peak (VV/VH) for both 12 mW and 5 mW. The intensity ratio for D peak is found to be 1.03 for 5 mW and 2.38 for 12 mW.

This shows that there is a polarization effect for D peak at 12 mW but not at 5 mW due to 8.5 mW threshold of enhanced emission on the wrinkle. We also studied the polarization dependent Raman spectra to prove that the VV and VH setups provided us with the parallel and perpendicular polarization PL spectra, respectively, in Figure S6. Raman spectra in the VH setup do not contain A<sub>1g</sub> modes.

#### **Discussions**

In the thermally-annealed multilayer MoS<sub>2</sub>, we also observed the enhanced emission for a defect level near 784 nm as shown in Figure S7. However, there is no enhanced emission from the defect levels when both PLs from Vs defect (labeled as D<sub>1</sub> in Figure S8) and one near 810 nm (labeled as D<sub>2</sub>) appear in multilayer MoS<sub>2</sub> near the edge of 210 nm sample in Fig. 1a, due to the splitting of electrons from Kc to two defect levels. The intensity ratio of D<sub>1</sub>/I<sub>1</sub> decreases while D<sub>2</sub>/I<sub>1</sub> increases linearly with the increasing laser power in Figure S8. The defects in thermally-annealed multilayer MoS<sub>2</sub> are stable and the observed enhanced emission is reproducible after the sample was kept in lab atmospheric condition for 10 months and re-measured. In a thin sample MoS<sub>2</sub> with a thickness of 25 nm, peaks near 583 nm that are related to a burned sample<sup>38</sup>, have been observed when the laser power reached 8 mW, as shown in Figure S9. Based on our observation, the optimal thickness range for achieving enhanced emission is between 25 nm and 360 nm. The safe operational window for laser powers is up to 30 mW for the thermally-annealed multilayer MoS<sub>2</sub>.

The safe operation window for laser powers is up to 22 mW for the UV laser irradiated multilayer MoS<sub>2</sub> as shown in Figure S10 where the optical image shows a burned sample under a laser power of 24 mW. In another UV-irradiated multilayer MoS<sub>2</sub> with a thickness of 89 nm, the

laser power of up to 25 mW can be used for the enhanced emission as shown in Figure S11. These UV-induced effects have been stable for 14 months. The lower operation window for laser powers in UV laser induced defects than in thermally annealing-induced ones is due to the existence of defects closer to the sample surface. After 14 months, the sample in Fig. 3 and 4 was cooled down to 103 K and warmed up to room temperature. The enhanced emission from defects of such a sample is reproducible as shown in Figure S10. In a UV-irradiated multilayer MoS<sub>2</sub> with a thickness of 10 nm, the sample was burned under a laser power of 5 mW (Figure S12). The optimal thickness range for achieving enhanced emission from UV-induced defect is expected between 35

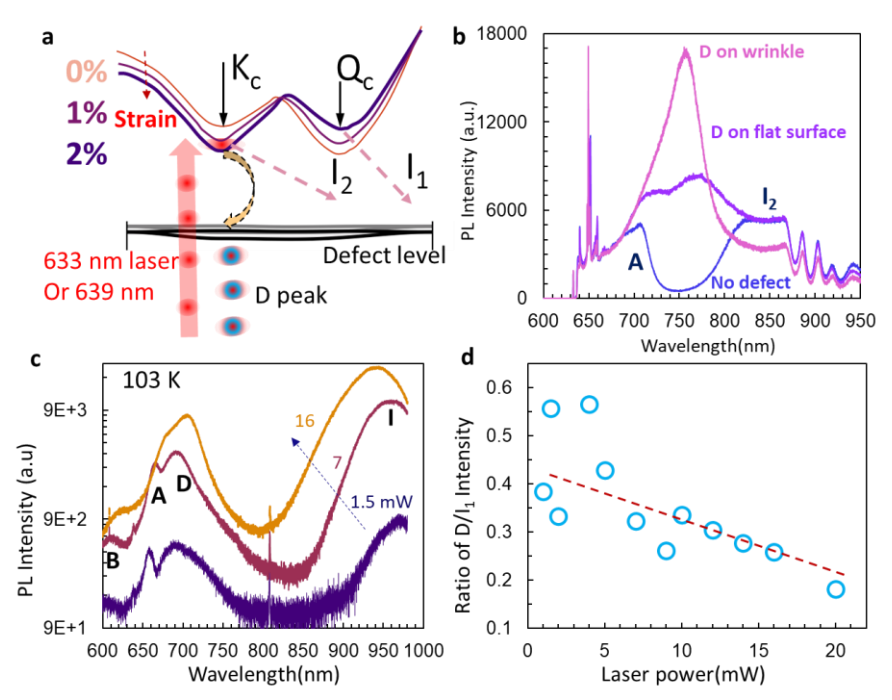


**Figure 6.** (a) Schematic of the band structure of bulk MoS<sub>2</sub> under different thermal strains. The 633 nm or 639 nm laser can pump electrons to K<sub>c</sub> only. (b) PL spectra from a multilayer MoS<sub>2</sub> without defects (dark blue line), with defects in flat region (dark purple line) and with defects in a wrinkle with a mechanic strain (pink line), excited by 633 nm. (c) PL spectra of UV laser irradiation-induced defects in flat multilayer MoS<sub>2</sub> at 103 K, excited by 532 nm laser. (d) The ratio of D peak to I<sub>1</sub> peak intensity, computed via peak fitting, as a function of laser powers.

(i.e. 25+10) nm and 350 (i.e. 360-10) nm.

A more detailed computational analysis leads to further experimental studies below. Figure 6a shows a schematic of the multilayer MoS2 band structure based on our previous work (see Fig.S11 of Ref. [29]). The band structures for increasing strain are plotted in darker colors. The strain engineering has resulted in a cross-over of Kc and Qc (i.e the energy level of Kc is lower than Qc for bulk MoS2 under thermal strains). As shown in the diagram, a carefully selected excitation laser (using 633 nm in PL and 639 nm in FLIM) pumps the electron to K<sub>c</sub> valley only. Above the threshold strain, the pristine  $Q_C-\Gamma_V$  (I<sub>1</sub>) indirect bandgap crosses over to the  $K_C-\Gamma_V$  (I<sub>2</sub>) indirect bandgap, resulting in more effective carrier relaxation from  $K_C$  valley to the defect level<sup>29</sup>. We next consider another possibility of pumping carriers only to the K<sub>C</sub> valley which eliminates I<sub>1</sub> from the PL spectrum and potentially allows carriers to relax more efficiently to the defect level. So, we studied the PL spectra by exciting MoS<sub>2</sub> with a 633 nm laser that is close to the fundamental gap between the conduction band minimum and the valence band maximum in our multilayer MoS<sub>2</sub> under different conditions. Figure 6b shows the PL spectra from our multilayer MoS<sub>2</sub> without defects (dark blue line), with defects in flat region (dark purple line), and with defects in a wrinkle with a mechanic strain (pink line), excited by 633 nm laser. There is no I<sub>1</sub> emission in all PLs because there is no carrier in the Qc valley. In the sample with defects, A-peak has a similar intensity as I<sub>2</sub> emission. D-peak has a higher intensity than the I<sub>2</sub> emission in the flat sample. With a strain in the wrinkle, the D peak is dominating in the PL, and I<sub>2</sub> emission has a less intensity than those in samples without the mechanic strain.

To further test the thermal-strain effect, we cool down the multilayer MoS<sub>2</sub> in Fig. 3 to 103 K. Fig. 6c shows PL spectra of UV laser irradiation-induced defects under laser powers of 1.5, 7, and 16 mW of 532 nm laser. Fig. 6d shows the decreasing ratio of D peak to I<sub>1</sub> peak intensity with increasing laser powers. There is no enhanced emission when the sample is at 103 K. The same sample shows the enhanced emission at room temperature in Figure S10, measured after Fig. 6c

and 6d. These results indicate that thermal strain in MoS<sub>2</sub> at the low temperature is not high enough for the cross-over of Kc and Qc.

To get the lifetime of the carrier, we studied the fluorescence lifetime imaging (FLIM) of the wrinkle region. Figure S13 shows an optical image of the wrinkle. Figure 7a and b show the FLIM measurement of the A and D peaks respectively in the wrinkle when the PL is excited by a 405 nm laser. The corresponding lifetime histogram is shown in Figure 7c where the lifetimes for A and D peak are 1.15 and 1.29 ns respectively. Under 639 nm laser excitation, the FLIM measurement of the wrinkle region for A and D peaks and the corresponding lifetime histogram are shown in Figures 7d-f respectively. The lifetime is measured to be 6.56 ns for D peak and 1.26

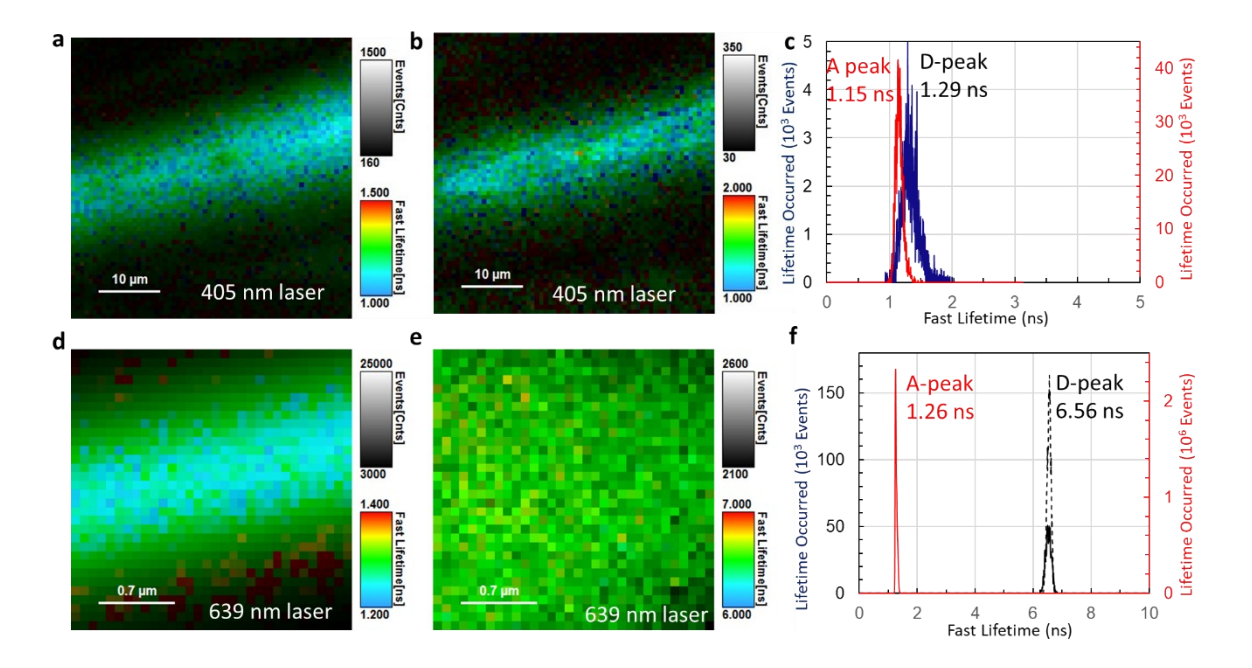


**Figure 7.** (a) FLIM measurement of the wrinkle region using 700±20 nm bandpass filter when the PL is excited by 405 nm laser. (b) FLIM measurement of the wrinkle region using 750±20 nm bandpass filter when the PL is excited by 405 nm laser. (c) Lifetime histogram obtained from FLIM when the PL is excited by 405 nm laser. (d) FLIM measurement of the whole wrinkle region using 700±20 nm bandpass filter when the PL is excited by 639 nm laser. (e) FLIM measurement of the whole wrinkle region using 750±20 nm bandpass filter when the PL is excited by 639 nm laser. (f) Lifetime histogram obtained from FLIM when the PL is excited by 639 nm laser.

ns for the A peak as shown in Figure 7f. The dashed and solid blue lines are data from two different measurements for the check of reproducibility. Achieving population inversion necessitates a difference in lifetime between competing excited states, and the presence of these two distinct peaks in the lifetime histogram strongly indicates such a difference. The FLIM unequivocally reveals the existence of enhanced emission from the D peak, consistent with our earlier findings.

In the future, a carefully selected laser can pump electrons to Kc only then the electrons jump from Kc to the point defects by integrating a resonant cavity with the sample, resulting in single photon emission (SPE) with high brightness<sup>39</sup>. To achieve the SPE, defects are created in vacuum, primarily associated with un-passivated Vs. (only Vs defects are observed in UV-irradiated multilayer MoS<sub>2</sub> in this study). The defect density should be controlled by adjusting the laser power or exposure time. The beam control and manipulation of UV laser are easier than the ion beam. Recently we applied UV laser to the sample through an objective lens. Finding the relationship between the defect peak strength and the Gaussian distribution of UV laser power is very efficient. In multilayer MoS<sub>2</sub>, raising the temperature instead of cooling down the sample might be necessary to observe the SPE. Deterministic strain patterning in multilayer MoS<sub>2</sub> will be a challenge. Another challenge is to characterize the defects at the atomic level. The scanning tunneling microscope (STM) <sup>34</sup> and dark-field scanning transmission electron microscopy (ADF-STEM)<sup>40</sup> imaging are effective in characterizing defects in monolayer MoS<sub>2</sub>. It is challenging to locate the defects in bulk MoS<sub>2</sub> for STM and ADF-STEM.

#### **Summary**

In this study, we have generated and studied S vacancies in multilayer MoS<sub>2</sub> through thermal annealing and through UV 375 nm laser irradiation. Our study of the defects in the bulk

underscores the profound influence of sample thickness on the thermal strain enabled enhanced

emission. Even though the thick samples absorb more temperatures, enhanced emission occurs

only within a limited thickness of the sample. The laser threshold for enhanced emission from

surface defects is observed to have a lower value compared to the bulk defects. The threshold can

be further reduced if we could combine mechanical strain with the thermal strain. When an

excitation near the fundamental bandgap is applied to the defect on wrinkles, we can make the

defect emission prominent in the PL spectra by eliminating the indirect I<sub>1</sub> emission. Such an

excitation would also increase the lifetime of enhanced emission by 5 times that of the A peak

emission.

**Supporting Information** 

Laser power and sample thickness-dependent Raman Spectra from flat and strained multilayer

MoS2, optical images from beam profilometer, polarization-dependent Raman spectra, PL spectra

under laser powers, PL spectra from a sample with two defect lines under different laser powers.

PL spectra of thin samples with thicknesses of 25 nm and 10 nm., PL spectra for checking the

defect stability and reproducibility of enhanced emission.

ORCID iDs

Yan Jiang https://orcid.org/0000-0003-0054-5193

Roberto Gonzalez Rodriguez https://orcid.org/0000-0001-6849-1799

Hao Yan https://orcid.org/ 0000-0003-1545-1659

Yuanxi Wang https://orcid.org/0000-0002-0659-1134

Anupama B. Kaul https://orcid.org/0000-0003-4052-8064

Jingbiao Cui https://orcid.org/0000-0003-3408-1016

Yuankun Lin https://orcid.org/0000-0001-5691-589X

21

### Acknowledgment

J.C. and Y.L. acknowledges partial financial support from U.S. National Science Foundation, grant number 2128367. A.K. and Y.L. acknowledge partial financial support by the Department of Energy/National Nuclear Security Administration under Award Number DE-NA0004114. Y.W. acknowledges startup funds from UNT and partial support from NSF DMR-2340733.

#### References

- (1) Iff, O.; Buchinger, Q.; Moczała-Dusanowska, M.; Kamp, M.; Betzold, S.; Davanco, M.; Srinivasan, K.; Tongay, S.; Antón-Solanas, C.; Höfling, S.; Schneider, C. Purcell-Enhanced Single Photon Source Based on a Deterministically Placed WSe 2 Monolayer Quantum Dot in a Circular Bragg Grating Cavity. *Nano Lett* **2021**, *21* (11), 4715–4720. https://doi.org/10.1021/acs.nanolett.1c00978.
- (2) Klein, J.; Sigl, L.; Gyger, S.; Barthelmi, K.; Florian, M.; Rey, S.; Taniguchi, T.; Watanabe, K.; Jahnke, F.; Kastl, C.; Zwiller, V.; Jöns, K. D.; Müller, K.; Wurstbauer, U.; Finley, J. J.; Holleitner, A. W. Engineering the Luminescence and Generation of Individual Defect Emitters in Atomically Thin MoS<sub>2</sub>. *ACS Photonics* **2021**, *8* (2), 669–677. https://doi.org/10.1021/acsphotonics.0c01907.
- (3) Iff, O.; Tedeschi, D.; Martín-Sánchez, J.; Moczała-Dusanowska, M.; Tongay, S.; Yumigeta, K.; Taboada-Gutiérrez, J.; Savaresi, M.; Rastelli, A.; Alonso-González, P.; Höfling, S.; Trotta, R.; Schneider, C. Strain-Tunable Single Photon Sources in WSe<sub>2</sub>Monolayers. *Nano Lett* **2019**, *19* (10), 6931–6936. https://doi.org/10.1021/acs.nanolett.9b02221.
- (4) Gao, H.; Suh, J.; Cao, M. C.; Joe, A. Y.; Mujid, F.; Lee, K. H.; Xie, S.; Xie, S.; Lee, J. U.; Kang, K.; Kim, P.; Muller, D. A.; Park, J. Tuning Electrical Conductance of MoS<sub>2</sub>Monolayers through Substitutional Doping. *Nano Lett* **2020**, *20* (6), 4095–4101. https://doi.org/10.1021/acs.nanolett.9b05247.
- (5) Zhang, F.; Zheng, B.; Sebastian, A.; Olson, D. H.; Liu, M.; Fujisawa, K.; Pham, Y. T. H.; Jimenez, V. O.; Kalappattil, V.; Miao, L.; Zhang, T.; Pendurthi, R.; Lei, Y.; Elías, A. L.; Wang, Y.; Alem, N.; Hopkins, P. E.; Das, S.; Crespi, V. H.; Phan, M.; Terrones, M. Monolayer Vanadium-Doped Tungsten Disulfide: A Room-Temperature Dilute Magnetic Semiconductor. *Advanced Science* 2020, 7 (24), 2198–3844. https://doi.org/10.1002/advs.202001174.
- (6) Sangwan, V. K.; Lee, H. S.; Bergeron, H.; Balla, I.; Beck, M. E.; Chen, K. S.; Hersam, M. C. Multi-Terminal Memtransistors from Polycrystalline Monolayer Molybdenum Disulfide. *Nature* **2018**, *554* (7693), 500–504. https://doi.org/10.1038/nature25747.

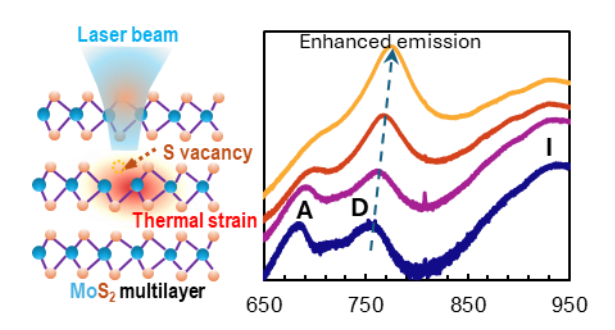
- (7) Ge, R.; Wu, X.; Kim, M.; Shi, J.; Sonde, S.; Tao, L.; Zhang, Y.; Lee, J. C.; Akinwande, D. Atomristor: Nonvolatile Resistance Switching in Atomic Sheets of Transition Metal Dichalcogenides. *Nano Lett* **2018**, *18* (1), 434–441. https://doi.org/10.1021/acs.nanolett.7b04342.
- (8) Xu, R.; Jang, H.; Lee, M. H.; Amanov, D.; Cho, Y.; Kim, H.; Park, S.; Shin, H. J.; Ham, D. Vertical MoS<sub>2</sub> Double-Layer Memristor with Electrochemical Metallization as an Atomic-Scale Synapse with Switching Thresholds Approaching 100 MV. *Nano Lett* **2019**, *19* (4), 2411–2417. https://doi.org/10.1021/acs.nanolett.8b05140.
- (9) Parto, K.; Azzam, S. I.; Banerjee, K.; Moody, G. Defect and Strain Engineering of Monolayer WSe<sub>2</sub> Enables Site-Controlled Single-Photon Emission up to 150 K. *Nat Commun* **2021**, *12* (1). https://doi.org/10.1038/s41467-021-23709-5.
- (10) Branny, A.; Kumar, S.; Proux, R.; Gerardot, B. D. Deterministic Strain-Induced Arrays of Quantum Emitters in a Two-Dimensional Semiconductor. *Nat Commun* **2017**, 8, 1–7. https://doi.org/10.1038/ncomms15053.
- (11) Grosso, G.; Moon, H.; Lienhard, B.; Ali, S.; Efetov, D. K.; Furchi, M. M.; Jarillo-Herrero, P.; Ford, M. J.; Aharonovich, I.; Englund, D. Tunable and High-Purity Room Temperature Single-Photon Emission from Atomic Defects in Hexagonal Boron Nitride. *Nat Commun* **2017**, *8* (1), 705–713. https://doi.org/10.1038/s41467-017-00810-2.
- (12) Branny, A.; Wang, G.; Kumar, S.; Robert, C.; Lassagne, B.; Marie, X.; Gerardot, B. D.; Urbaszek, B. Discrete Quantum Dot like Emitters in Monolayer MoSe<sub>2</sub>: Spatial Mapping, Magneto-Optics, and Charge Tuning. *Appl Phys Lett* **2016**, *108* (14), 1–6. https://doi.org/10.1063/1.4945268.
- (13) Hus, S. M.; Ge, R.; Chen, P. A.; Liang, L.; Donnelly, G. E.; Ko, W.; Huang, F.; Chiang, M. H.; Li, A. P.; Akinwande, D. Observation of Single-Defect Memristor in an MoS<sub>2</sub> Atomic Sheet. *Nat Nanotechnol* **2021**, *16* (1), 58–62. https://doi.org/10.1038/s41565-020-00789-w.
- (14) Chakraborty, C.; Kinnischtzke, L.; Goodfellow, K. M.; Beams, R.; Vamivakas, A. N. Voltage-Controlled Quantum Light from an Atomically Thin Semiconductor. *Nat Nanotechnol* **2015**, *10* (6), 507–511. https://doi.org/10.1038/nnano.2015.79.
- (15) Klein, J.; Lorke, M.; Florian, M.; Sigger, F.; Sigl, L.; Rey, S.; Wierzbowski, J.; Cerne, J.; Müller, K.; Mitterreiter, E.; Zimmermann, P.; Taniguchi, T.; Watanabe, K.; Wurstbauer, U.; Kaniber, M.; Knap, M.; Schmidt, R.; Finley, J. J.; Holleitner, A. W. Site-Selectively Generated Photon Emitters in Monolayer MoS<sub>2</sub> via Local Helium Ion Irradiation. *Nat Commun* **2019**, *10* (1), 1–8. https://doi.org/10.1038/s41467-019-10632-z.
- (16) Barthelmi, K.; Klein, J.; Hötger, A.; Sigl, L.; Sigger, F.; Mitterreiter, E.; Rey, S.; Gyger, S.; Lorke, M.; Florian, M.; Jahnke, F.; Taniguchi, T.; Watanabe, K.; Zwiller, V.; Jöns, K. D.; Wurstbauer, U.; Kastl, C.; Weber-Bargioni, A.; Finley, J. J.; Müller, K.; Holleitner, A. W. Atomistic Defects as Single-Photon Emitters in Atomically Thin MoS<sub>2</sub>. *Applied Physics Letters*. American Institute of Physics Inc. August 17, 2020, pp 1–7. https://doi.org/10.1063/5.0018557.
- (17) Chakraborty, C.; Goodfellow, K. M.; Nick Vamivakas, A. Localized Emission from Defects in MoSe<sub>2</sub> Layers. *Opt Mater Express* **2016**, *6* (6), 2081–2087. https://doi.org/10.1364/ome.6.002081.

- (18) Luo, Y.; Shepard, G. D.; Ardelean, J. V.; Rhodes, D. A.; Kim, B.; Barmak, K.; Hone, J. C.; Strauf, S. Deterministic Coupling of Site-Controlled Quantum Emitters in Monolayer WSe<sub>2</sub> to Plasmonic Nanocavities. *Nature Nanotechnology*. Nature Publishing Group December 1, 2018, pp 1137–1142. https://doi.org/10.1038/s41565-018-0275-z.
- (19) Dang, J.; Sun, S.; Xie, X.; Yu, Y.; Peng, K.; Qian, C.; Wu, S.; Song, F.; Yang, J.; Xiao, S.; Yang, L.; Wang, Y.; Rafiq, M. A.; Wang, C.; Xu, X. Identifying Defect-Related Quantum Emitters in Monolayer WSe<sub>2</sub>. *npj* 2D Materials and Applications 1 2020, 4 (1), 1–7. https://doi.org/10.1038/s41699-020-0136-0.
- (20) Schuler, B.; Cochrane, K. A.; Kastl, C.; Barnard, E. S.; Wong, E.; Borys, N. J.; Schwartzberg, A. M.; Ogletree, D. F.; de Abajo, F. J. G.; Weber-Bargioni, A. Electrically Driven Photon Emission from Individual Atomic Defects in Monolayer WS 2. *Sci Adv* **2020**, *6* (38), 1–7. https://doi.org/10.1126/sciadv.abb5988.
- (21) Palacios-Berraquero, C.; Kara, D. M.; Montblanch, A. R. P.; Barbone, M.; Latawiec, P.; Yoon, D.; Ott, A. K.; Loncar, M.; Ferrari, A. C.; Atatüre, M. Large-Scale Quantum-Emitter Arrays in Atomically Thin Semiconductors. *Nat Commun* **2017**, *8*, 1–6. https://doi.org/10.1038/ncomms15093.
- (22) Zhao, H.; Pettes, M. T.; Zheng, Y.; Htoon, H. Site-Controlled Telecom-Wavelength Single-Photon Emitters in Atomically-Thin MoTe<sub>2</sub>. *Nat Commun* **2021**, *12* (1), 6753–6760. https://doi.org/10.1038/s41467-021-27033-w.
- (23) Shaik, A. B. D.; Palla, P. Optical Quantum Technologies with Hexagonal Boron Nitride Single Photon Sources. *Sci Rep* **2021**, *11* (1), 12285–12312. https://doi.org/10.1038/s41598-021-90804-4.
- (24) Tran, T. T.; Bray, K.; Ford, M. J.; Toth, M.; Aharonovich, I. Quantum Emission from Hexagonal Boron Nitride Monolayers. *Nat Nanotechnol* **2016**, *11* (1), 37–41. https://doi.org/10.1038/nnano.2015.242.
- (25) Tonndorf, P.; Del Pozo-Zamudio, O.; Gruhler, N.; Kern, J.; Schmidt, R.; Dmitriev, A. I.; Bakhtinov, A. P.; Tartakovskii, A. I.; Pernice, W.; Michaelis de Vasconcellos, S.; Bratschitsch, R. On-Chip Waveguide Coupling of a Layered Semiconductor Single-Photon Source. *Nano Lett* **2017**, *17* (9), 5446–5451. https://doi.org/10.1021/acs.nanolett.7b02092.
- (26) Tonndorf, P.; Schwarz, S.; Kern, J.; Niehues, I.; Del Pozo-Zamudio, O.; Dmitriev, A. I.; Bakhtinov, A. P.; Borisenko, D. N.; Kolesnikov, N. N.; Tartakovskii, A. I.; Michaelis de Vasconcellos, S.; Bratschitsch, R. Single-Photon Emitters in GaSe. *2d Mater* **2017**, *4* (2), 1–7. https://doi.org/10.1088/2053-1583/aa525b.
- (27) Tran, T. T.; Choi, S.; Scott, J. A.; Xu, Z.; Zheng, C.; Seniutinas, G.; Bendavid, A.; Fuhrer, M. S.; Toth, M.; Aharonovich, I. Room-Temperature Single-Photon Emission from Oxidized Tungsten Disulfide Multilayers. *Adv Opt Mater* **2017**, *5* (5), 1–13. https://doi.org/10.1002/adom.201600939.
- (28) Wang, W.; Jones, L. O.; Chen, J. S.; Schatz, G. C.; Ma, X. Utilizing Ultraviolet Photons to Generate Single-Photon Emitters in Semiconductor Monolayers. *ACS Nano* **2022**, *16* (12), 21240–21247. https://doi.org/10.1021/acsnano.2c09209.

- (29) Lin, Y.; Hathaway, E.; Habis, F.; Wang, Y.; Rodriguez, R. G.; Alnasser, K.; Hurley, N.; Cui, J. Enhanced Emission from Defect Levels in Multilayer MoS<sub>2</sub>. *Adv Opt Mater* **2022**, *10* (19), 1–9. https://doi.org/10.1002/adom.202201059.
- (30) Tran Khac, B. C.; Jeon, K.-J.; Choi, S. T.; Kim, Y. S.; DelRio, F. W.; Chung, K.-H. Laser-Induced Particle Adsorption on Atomically Thin MoS<sub>2</sub>. *ACS Appl Mater Interfaces* **2016**, *8* (5), 2974–2984. https://doi.org/10.1021/acsami.5b09382.
- (31) Castellanos-Gomez, A.; Barkelid, M.; Goossens, A. M.; Calado, V. E.; van der Zant, H. S. J.; Steele, G. A. Laser-Thinning of MoS 2: On Demand Generation of a Single-Layer Semiconductor. *Nano Lett* **2012**, *12* (6), 3187–3192. https://doi.org/10.1021/nl301164v.
- (32) Tran-Khac, B.-C.; White, R. M.; DelRio, F. W.; Chung, K.-H. Layer-by-Layer Thinning of MoS via Laser Irradiation. *Nanotechnology* **2019**, *30* (27), 1–15. https://doi.org/10.1088/1361-6528/ab11ad.
- (33) Alrasheed, A.; Gorham, J. M.; Tran Khac, B. C.; Alsaffar, F.; DelRio, F. W.; Chung, K.-H.; Amer, Moh. R. Surface Properties of Laser-Treated Molybdenum Disulfide Nanosheets for Optoelectronic Applications. *ACS Appl Mater Interfaces* **2018**, *10* (21), 18104–18112. https://doi.org/10.1021/acsami.8b04717.
- (34) Mitterreiter, E.; Schuler, B.; Micevic, A.; Hernangómez-Pérez, D.; Barthelmi, K.; Cochrane, K. A.; Kiemle, J.; Sigger, F.; Klein, J.; Wong, E.; Barnard, E. S.; Watanabe, K.; Taniguchi, T.; Lorke, M.; Jahnke, F.; Finley, J. J.; Schwartzberg, A. M.; Qiu, D. Y.; Refaely-Abramson, S.; Holleitner, A. W.; Weber-Bargioni, A.; Kastl, C. The Role of Chalcogen Vacancies for Atomic Defect Emission in MoS<sub>2</sub>. Nat Commun 2021, 12 (1), 18. https://doi.org/10.1038/s41467-021-24102-y.
- (35) Sensoy, M. G.; Vinichenko, D.; Chen, W.; Friend, C. M.; Kaxiras, E. Strain Effects on the Behavior of Isolated and Paired Sulfur Vacancy Defects in Monolayer MoS<sub>2</sub>. *Phys Rev B* **2017**, 95 (1), 1–7. https://doi.org/10.1103/PhysRevB.95.014106.
- (36) Lin, Y.; Hurley, N.; Kamau, S.; Hathaway, E.; Jiang, Y.; Rodriguez, R. G.; Varghese, S.; Krylyuk, S.; Davydov, A. V.; Wang, Y.; Kaul, A.; Cui, J. Strain-Activated Stimulated Emission from Multilayer MoSe 2 in a Narrow Operation Window. *physica status solidi (RRL) Rapid Research Letters* **2024**, *18* (2), 1–8. https://doi.org/10.1002/pssr.202300343.
- (37) Dutta, N. K.; Craft, D. C. Effect of Stress on the Polarization of Stimulated Emission from Injection Lasers. *J Appl Phys* **1984**, *56* (1), 65–70. https://doi.org/10.1063/1.333764.
- (38) Hurley, N.; Bhandari, B.; Kamau, S.; Gonzalez Rodriguez, R.; Squires, B.; Kaul, A. B.; Cui, J.; Lin, Y. Selective CW Laser Synthesis of MoS2 and Mixture of MoS2 and MoO2 from (NH4)2MoS4 Film. *Micromachines (Basel)* **2024**, *15* (2), 258. https://doi.org/10.3390/mi15020258.
- (39) Wei, Y.; Liu, S.; Li, X.; Yu, Y.; Su, X.; Li, S.; Shang, X.; Liu, H.; Hao, H.; Ni, H.; Yu, S.; Niu, Z.; Iles-Smith, J.; Liu, J.; Wang, X. Tailoring Solid-State Single-Photon Sources with Stimulated Emissions. *Nat Nanotechnol* **2022**, *17* (5), 470–476. https://doi.org/10.1038/s41565-022-01092-6.

(40) Hong, J.; Hu, Z.; Probert, M.; Li, K.; Lv, D.; Yang, X.; Gu, L.; Mao, N.; Feng, Q.; Xie, L.; Zhang, J.; Wu, D.; Zhang, Z.; Jin, C.; Ji, W.; Zhang, X.; Yuan, J.; Zhang, Z. Exploring Atomic Defects in Molybdenum Disulphide Monolayers. *Nat Commun* **2015**, *6* (1), 6293. https://doi.org/10.1038/ncomms7293.

# For Table of Contents Only



**Supporting Information** 

Thermal-strain Enabled Enhanced Emission from UV

Laser-induced Defect Levels near the Surface of

Multilayer MoS<sub>2</sub>

Sinto Varghese <sup>1</sup>, Noah Hurley <sup>1</sup>, Steve Kamau <sup>1</sup>, Yan Jiang <sup>1</sup>, Roberto Gonzalez Rodriguez <sup>1</sup>,

Bhojraj Bhandari <sup>1</sup>, Tengteng Lyu <sup>2</sup>, Hao Yan <sup>2</sup>, Yuanxi Wang <sup>1</sup>, Anupama B. Kaul <sup>3,4</sup>, Jingbiao

Cui, and Yuankun Lin 1,3\*

<sup>1</sup>Department of Physics, University of North Texas, Denton, TX 76203, USA

<sup>2</sup>Department of Chemistry, University of North Texas, Denton, TX 76203, USA

<sup>3</sup>Department of Electrical Engineering, University of North Texas, Denton, TX 76203, USA

<sup>4</sup>Department of Materials Science and Engineering, University of North Texas, Denton, TX, USA

\* Corresponding author

E-mail: yuankun.lin@unt.edu

27

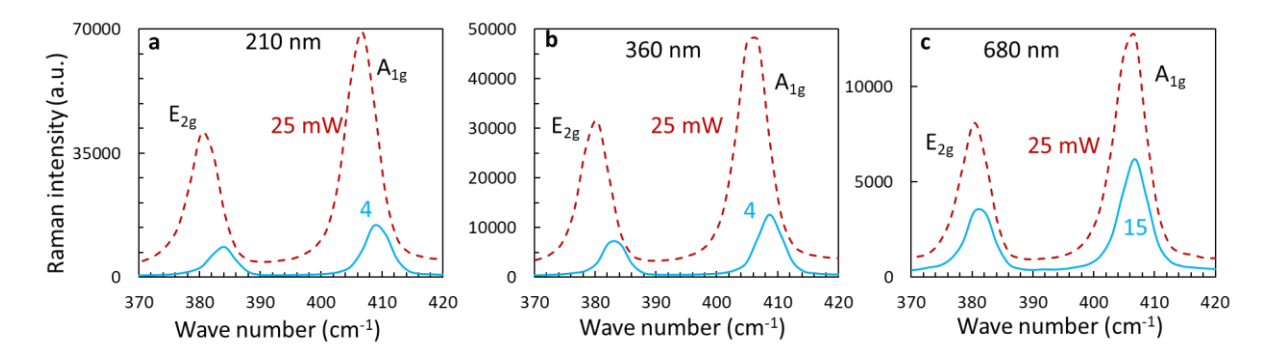


**Figure S2.** Raman spectra under laser power of 4 mW(blue) and 25 mW(red) for Multilayer MoS<sub>2</sub> of thickness (a) 210 nm (b) 360 nm (c) Raman spectra under laser power of 15 mW(blue) and 25 mW(red) for Multilayer MoS<sub>2</sub> of thickness 680 nm

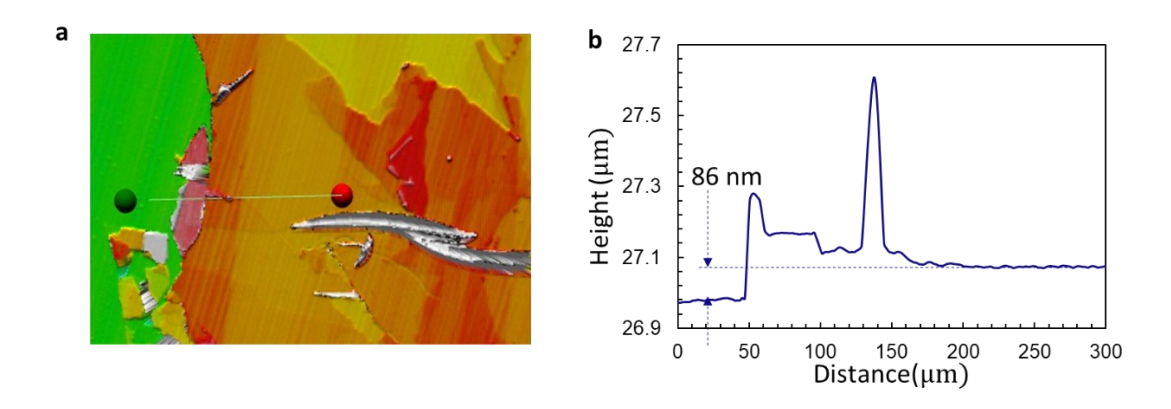


**Figure S2.** (a) Image of the sample surface of multilayer MoS<sub>2</sub> with flat and wrinkle region made by profilometer. (b) The profilometer measurements for calculating sample thickness.

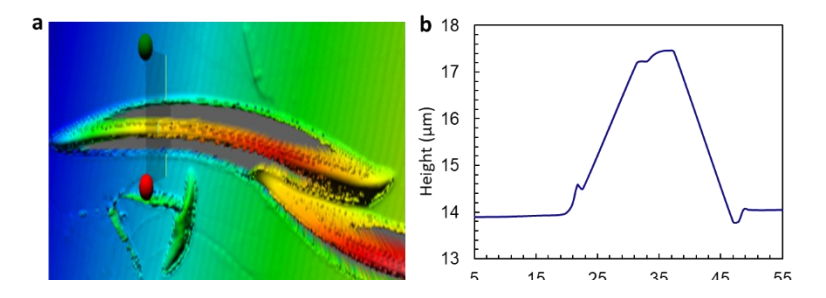


**Figure S3.** Optical image from profilometer for measuring height and width of the wrinkle in the multilayer MoS<sub>2</sub> (a) and the corresponding profiles (b).

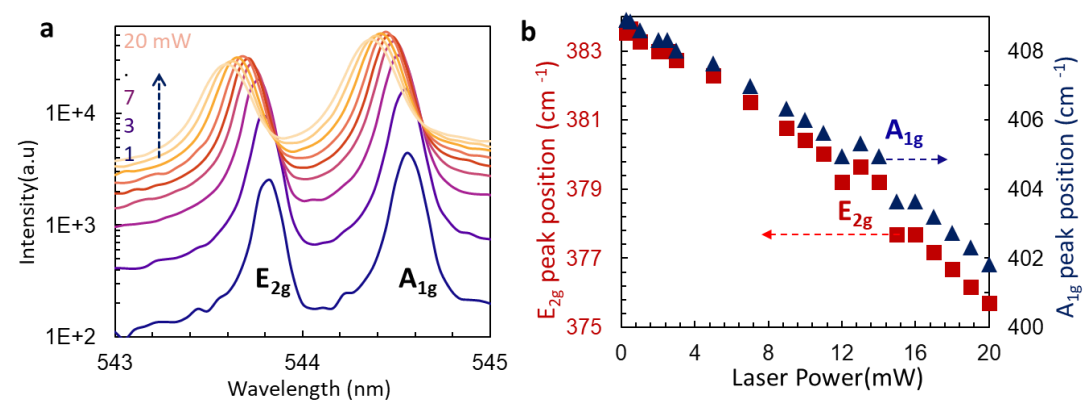


**Figure S4.** (a) Power dependent Raman spectra on the flat region of multilayer  $MoS_2$  at various laser powers of 0.25, 0.5, 1, 2, 2.5, 3, 5, 7, 9, 10, 11, 12, 13, 14, 15, 16, 17, 18, 19, and 20 mW. (b)Raman peak shift of  $E_{2g}$  and  $A_{1g}$  as we increased the laser power on the flat region of multilayer  $MoS_2$ . Blue colour represents  $A_{1g}$  peak and red colour represent  $E_{2g}$ 

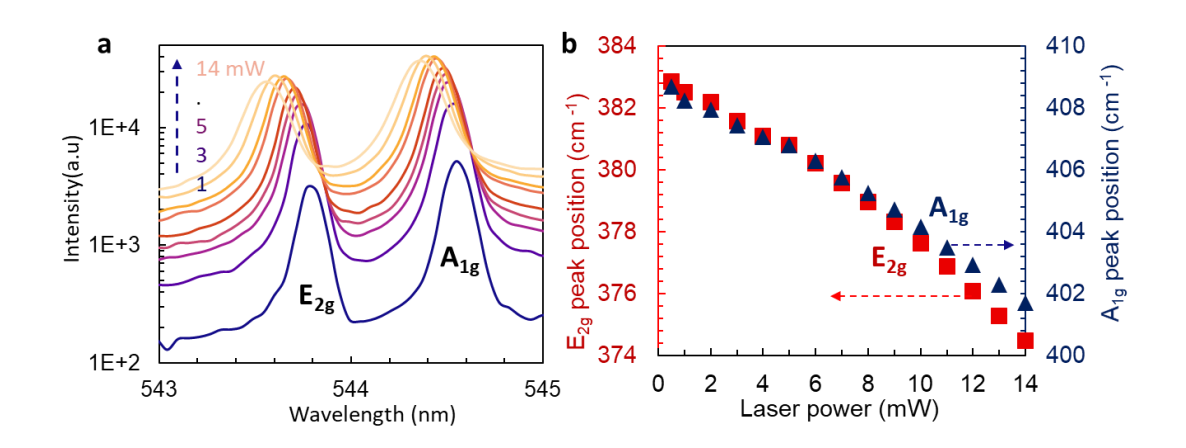


**Figure S5.** (a) Power dependent Raman spectra on the wrinkle region of multilayer  $MoS_2$  at various laser powers of from 0.5, 1, 2, 3, 4, 5, 6, 7, 8, 9, 10, 11, 12, 13, and 14 mW. (b)Raman peak shift of  $E_{2g}$  and  $A_{1g}$  as we increased the laser power on the flat region of multilayer  $MoS_2$ . Blue colour represents  $A_{1g}$  peak and red colour represent  $E_{2g}$  peak.

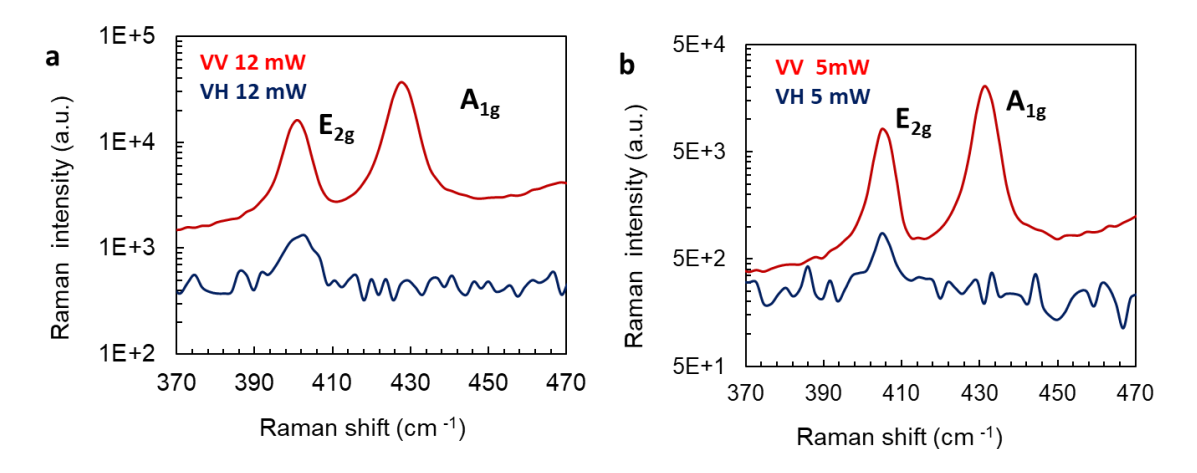


**Figure S6.** Polarization dependent Raman spectra in the wrinkle region of multilayer MoS<sub>2</sub> (a) at 12 mW and (b) at 5mW where red curve represents the parallel polarization (VV) and blue curve represents the perpendicular polarization (VH).

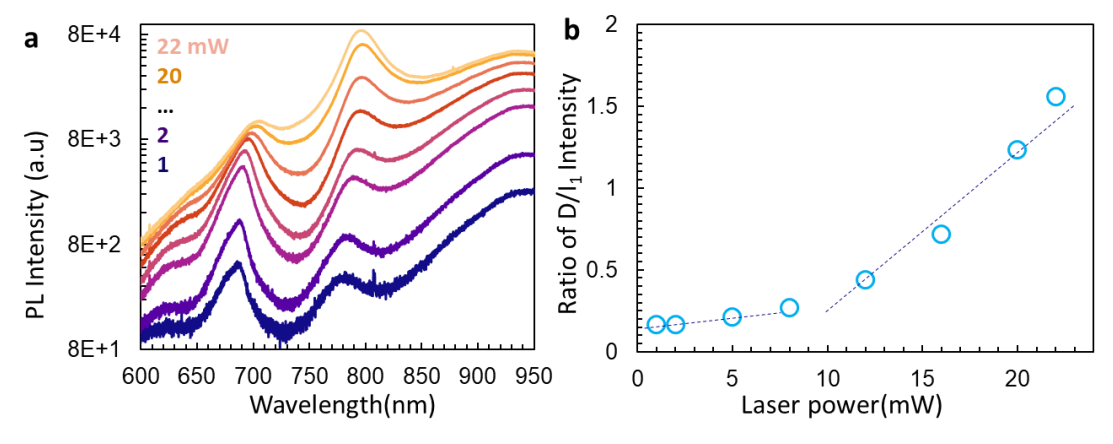


**Figure S7.** (a) PL spectra under laser powers of 1, 2, 5, 8, 12, 16, 20, and 22 mW from a different sample MoS<sub>2</sub> from Fig. 1a. (b) The ratio of D peak to I<sub>1</sub> peak as a function of laser powers.

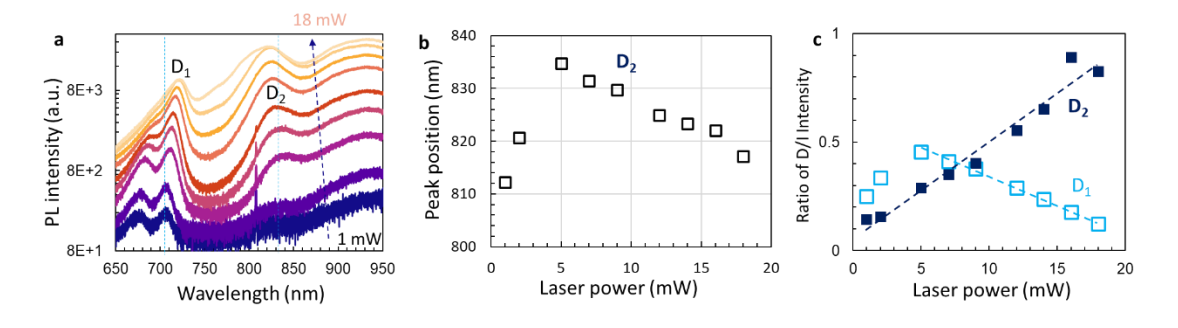


**Figure S8.** (a) PL spectra under laser powers of 1, 2, 5, 7, 9, 12, 14, 16, and 18 mW from an edge of 210 nm sample in Fig. 1a. (b)  $D_2$ -PL peak positions as a function of laser power. (c) The ratio of  $D_1$  ( $D_2$ ) peak to  $I_1$  intensity, computed via peak fitting, as a function of laser powers.

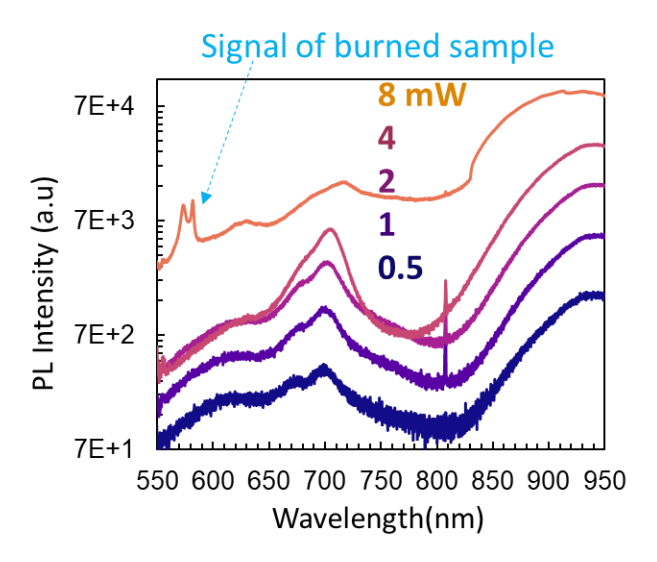


**Figure S9.** PL spectra under laser powers of 0.5,1, 2, 4, and 8 mW from thermally annealed multilayer MoS<sub>2</sub> with a thickness of 25 nm. The appearance of peaks near 583 nm is related to the burned sample<sup>1</sup>.

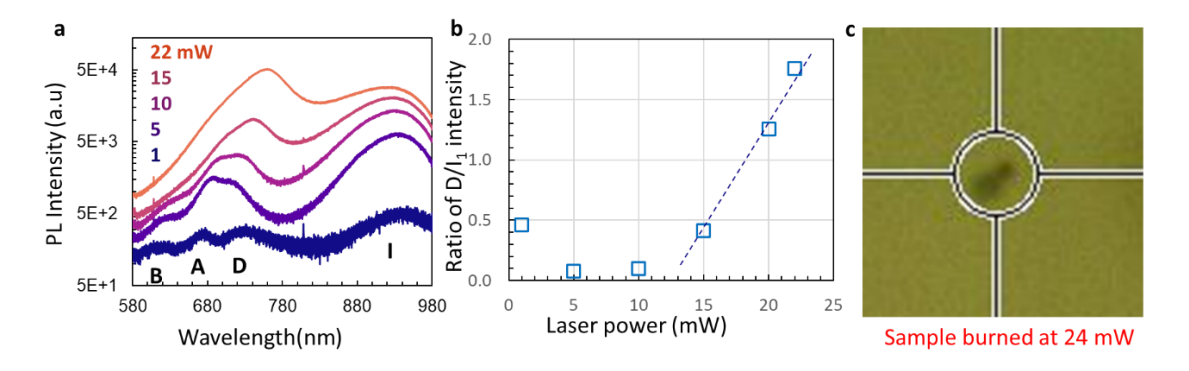


**Figure S10.** (a) PL spectra of UV laser irradiation-induced defects in flat multilayer MoS<sub>2</sub> with a thickness of 86 nm under laser powers of 1, 5, 10, 15, and 22 mW from bottom to top. The sample is 14 months old and has been cooled down to 103 K once. (b) The ratio of D peak to I<sub>1</sub> peak intensity, computed via peak fitting, as a function of laser powers. (c) Optical image of burned sample after an exposure to a laser power of 24 mW.

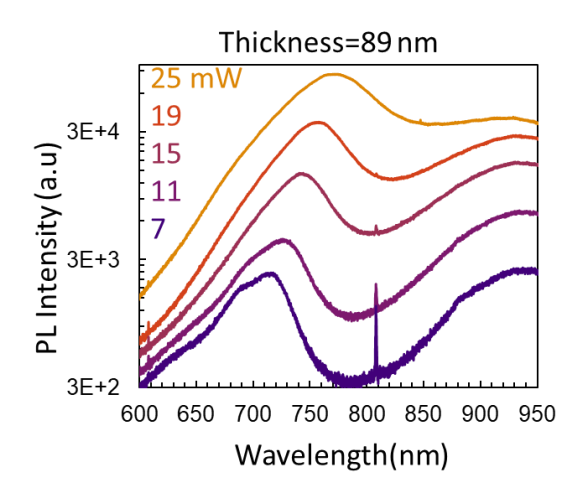


**Figure S11.** (a) PL spectra of UV laser irradiation-induced defects in flat multilayer MoS<sub>2</sub> with a thickness of 89 nm under laser powers of 7, 11,15, 19, and 25 mW from bottom to top.

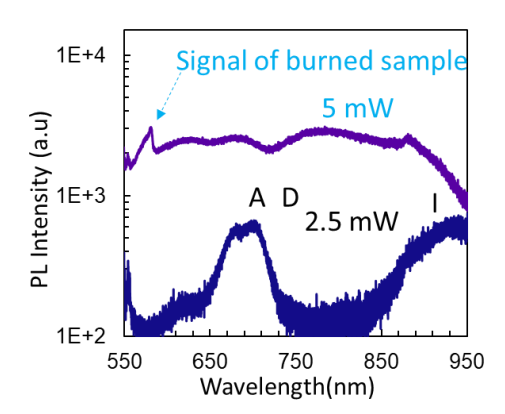


**Figure S12.** PL spectra of UV laser irradiation-induced defects in flat multilayer MoS<sub>2</sub> with a thickness of 10 nm under laser powers of 2.5, and 5 mW from bottom to top. The appearance of the peak near 583 nm indicates that the sample is burned under 5 mW<sup>1</sup>.

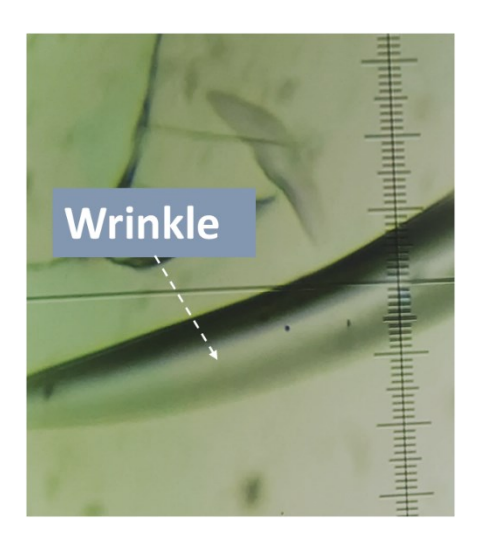


Figure S13. (a) Optical image of the wrinkle from multilayer MoS<sub>2</sub> sample.

## Reference:

1. Hurley, N.; Bhandari, B.; Kamau, S.; Gonzalez Rodriguez, R.; Squires, B.; Kaul, A.B.; Cui, J.; Lin, Y. Selective CW Laser Synthesis of MoS<sub>2</sub> and Mixture of MoS<sub>2</sub> and MoO<sub>2</sub> from (NH<sub>4</sub>)<sub>2</sub>MoS<sub>4</sub> Film. *Micromachines* **2024**, *15*, 258. https://doi.org/10.3390/mi15020258